Silicon Nanowire Arrays Coated with Ag and Au Dendrites for Surface-Enhanced Raman Scattering

Nikita Grevtsov[1], Aliaksandr Burko[1], Sergey Redko[1], Nadzeya Khinevich[1,2], Siarhei Zavatski[1,3], Stanislau Niauzorau[4], Hanna Bandarenka[1,4]

[1] Micro- and Nanoelectronics Department, Belarusian State University of Informatics and Radioelectronics, Minsk, Belarus

[2] Institute of Materials Science, Kaunas University of Technology, Kaunas, Lithuania

[3] Nanophotonics and Metrology Laboratory, Swiss Federal Institute of Technology Lausanne (EPFL), Lausanne 1015, Switzerland

[4] The Polytechnic School, Arizona State University, Mesa, AZ, United States

Silicon nanowires (SiNWs) were comprehensively characterized in dependence on conditions of their formation via metal (Ag) -assisted chemical etching (MACE) of monocrystalline Si. The Ag structures remained on/between SiNWs based on both n- and p-Si were found to promote surface enhancement of Raman scattering (SERS) from organic molecules adsorbed on their surface. The Ag structures on/between the SiNWs/p-Si facilitated two times higher SERS-signal from 10^{-6} M rhodamine 6G than those in the SiNWs/n-Si. The activity of the SERS-substrates based on p-Si was improved by modification with small Au dendrites, which provided rich family of hot spots and prevented degradation of the SERS-activity observed for pure Ag dendrites due to formation of Ag_2S during one week of storage in air. The SERS-substrates based on the Au/Ag dendrites on SiNWs/p-Si allowed to achieve nanomolar detection limit of rhodamine 6G and 5,5'-dithiobis (2-nitrobenzoic acid).

INTRODUCTION

The MACE can be utilized to produce various semiconductor nanostructures, ranging from disordered porous layers to arrays of uniform vertically aligned SiNWs. In recent years, these SiNWs have been attracting a lot of interest due to their unique optical and mechanical properties associated with well-developed surface area, leading to their successful application in numerous areas including but not limited to energy sources [1–4], photovoltaics [5–8] and SERS-spectroscopy [9–10].

Out of all the methods currently available, two main MACE approaches can be distinguished. The first one (*a single-stage method*) is realized by immersing the Si wafer in a solution containing noble metal ions, oxidizing (e.g. H_2O_2) and etching (e.g. HF) agents. In such a case, Si etching and the deposition of metal particles occurs simultaneously. Due to the catalytic activity of noble metal particles, Si atoms located directly underneath them are oxidized with H_2O_2 to SiO_2, which is then dissolved in HF at a very high rate, leading to formation of pores in the Si wafer [11]. The second approach (*a two-stage method)* involves Si etching and metal particles deposition at the separate steps. This results in a more precise control over the SiNWs morphology compared with the single-stage method, although the latter one provides a faster porosification of Si [0]. It should be also emphasized that morphological parameters of resulting Si nanostructures strongly depend on a number of MACE conditions [12–20] that are listed and considered in the Section 1 of Supplementary Materials.

The SiNWs arrays serve as an attractive "host" material to form nanostructures of other "guest" materials. Their structural parameters can be adjusted to a specific application through managing the nanowires length, diameter, spatial location and dopant level. It has previously been reported that the SiNWs grown by the reactive ion etching and coated with noble metal nanoparticles demonstrate a prominent SERS-activity [21]. On the other hand, it has also been shown that the SERS-active substrates based on the nanostructured Si layers (porous Si) fabricated by wet electrochemical etching of the Si wafers and covered with Ag provide improved chemical stability of the Ag nanoparticles [22]. Inspired by these results, we aimed to fabricate and characterize SiNWs that exhibit both the strong stability and a great Raman signal enhancement. We did this through comprehensive examination of the process-structure-properties relationship for the SiNWs formed by the two-step MACE using Ag as a catalyst and different Si dopant types.

EXPERIMENTAL

Silver nitrate, $AgNO_3$ (ACS reagent, $\geq$ 99.0 %); gold(III) chloride trihydrate, $HAuCl_4 \cdot 3H_2O$ ($\geq$ 99.9 %); ethanol, C_2H_5OH (ACS reagent, $\geq$ 99.5 %); hydrofluoric acid, HF (48 wt. % in H_2O); hydrogen peroxide solution, H_2O_2 (ACS reagent, 30 wt. % in H_2O); nitric acid, HNO_3 (ACS reagent, 70 %); potassium dichromate, $K_2Cr_2O_7$ (ACS reagent, $\geq$ 99.0 %); sulfuric acid, H_2SO_4 (ACS reagent, 95.0–98.0 %); rhodamine 6G, R6G (99 %); 5,5′-dithiobis (2-nitrobenzoic acid), DTNB (99.0 %) were purchased from Sigma-Aldrich and used without additional purification. Four-inches Si wafers with 525 ± 15 µm thickness and <100> slice off orientation of Prime quality (Kamerton-Integral, Pinsk, Belarus) were lightly doped with phosphorous and boron, double side polished. Water was purified with Milli-Q system (Millipore, Bedford, MA, USA).

Fabrication of the experimental samples of SiNWs with Ag and Ag/Au dendrites is well-described in the Section 2 of Supplementary Materials.

To simulate an electric field distribution in the Ag dendrites on the layer of SiNWs we used AC/DC Module embedded in COMSOL Multiphysics 5.3a. A 3D frequency-domain wave equation was solved with a finite element method for the electric field to find its distribution in the silver structures. The SiNWs layer was assumed to have parameters of amorphous Si [23]. Ag optical properties for the simulations were extracted from [24]. An excitation light of 633 nm wavelength was simulated as a plane wave with a normal incidence in the full-field formulation. The light wave propagated in a negative y-direction. The incident power density was 10^5 W/cm^2 to be as close as possible to that used while the experimental SERS-measurements. The Floquet periodic boundary conditions were assigned for the all sidewalls. The minimum free triangular element size in the mesh was 26.5 nm.

The morphology and elemental analysis of the samples was studied with a scanning electron microscope Hitachi S-4800 (SEM; Hitachi, Tokyo, Japan) equipped with an energy-dispersive X-ray QUANTAX 200 analyzer (EDS; Bruker, Berlin, Germany). Reflectance spectra of the SiNWs samples free of silver residues were recorded using an MC122 spectrophotometer (Proscan Special Instruments, Minsk, Belarus) in a 350–1050 nm range. R6G dissolved in water and DTNB dissolved in ethanol were used as analytes for the SERS-measurements. The substrates based on the SiNWs containing silver structures and silver/gold dendrites were immersed into 1 ml of solution containing 10^{-6}–10^{-9} M analytes for 1 h and then rinsed to remove an excess of non-adsorbed molecules. We first prepared the basic solutions of the analytes with a 10^{-2} M concentration that was gradually decreased by successive dilution with the proper solvent. The analytes' SERS spectra were collected using a Confotec NR500 3D scanning Raman microscope (SOL Instruments Ltd., Minsk, Belarus). The SERS-measurements were carried out with a 633 nm He-Ne laser focused through the 40× objective (NA = 0.75). The laser spot diameter was calculated to be 1030 nm. Laser power density after losses in optical system and objective was $(1\pm0.2)\cdot10^5$ W/cm^2. Signal accumulation time was 1 s for all the samples.

RESULTS AND DISCUSSION

Morphology and reflectance of SiNWs

Figure 1 shows SEM images for the different SiNWs and Ag structures. Columns correspond to 0.5, 1, 3 or 10 min of Ag deposition time on the first MACE stage.
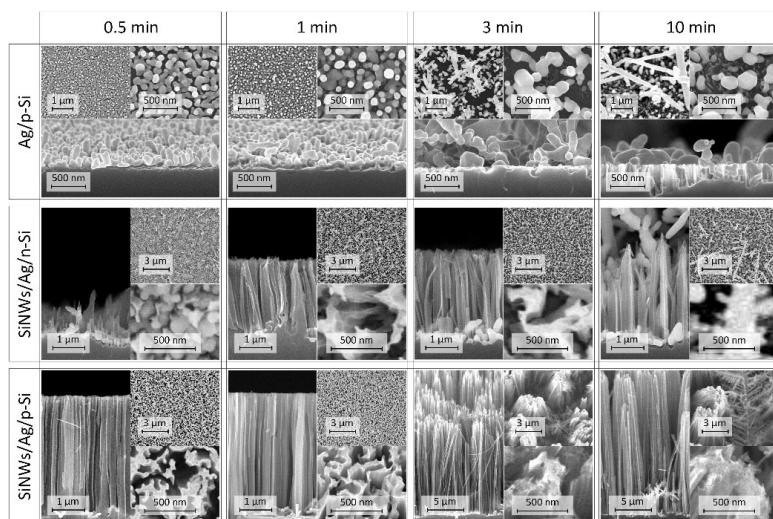
3

Figure 1 – SEM images for (top row) Ag structures deposited on *p*-Si on the first MACE stage, SiNWs etched in (middle row) *n*-Si and (bottom row) *p*-Si on the second MACE stage.

The first row reports silver-coated *p*-Si nanostructures, while the second and third rows show the SiNWs obtained after *n*-Si and *p*-Si etching, respectively. The SEM images for the silver-coated *n*-Si nanostructures are not presented because their morphology is nearly the same as for the silver-coated *p*-Si.

It is seen from Figure 1 that the higher deposition times on the first MACE stage induce Ag films transition from densely packed quasi-spherical and elongated Ag nanoparticles to slightly branched dendrites. The structural parameters of the Ag particles and dendrites are described in Section 3 of Supplementary Materials. Due to the presence of HF in the silver deposition solution, visible pores in the Si wafer are already observed after the first MACE stage. A growth mechanism of this porous layer is identical to that occurring during the second MACE stage and follows the standard Si etching kinetics. The silver films after 3 min and 10 min deposition exhibit dendritic morphology, which is evolve along with increase of the immersion time. The majority of silver mass in such samples is not in the contact with Si, and therefore do not directly participate in the etching process. Their presence, however, leads to the nanowires' formation with larger aspect ratios. An increase in the nanowires length along with the dendrite layer thickness can be attributed to the following factors. (i) A large volume of silver dendrites immersed in a H_2O_2 solution is oxidized, producing a great amount of Ag^+ ions, which are subsequently reduced to Ag^0 and redeposited [25]. Redeposition may occur both on the adjacent metal particles and on Si itself, including the areas deep within the pores [26]. (ii) Diffusion of holes (generated because of Ag redeposition) into the silver particles in contact with the wafer leads to a higher Si oxidation and etching rate [26]. (iii) The significant mass of dendrites means a closer adherence of underlying silver particles to the Si wafer. This may accelerate the holes diffusion between these particles and the wafer, resulting in a higher etching rate. After a certain point, however, the latter of these three factors can also become a limiting one since the thicker the dendrite layer becomes, the harder it is for the reagents (H_2O_2 and HF) and reaction byproducts to move between the

electrolyte volume and the wafer surface. With the reagent transfer occurring in the gap between the silver particles and the wafer, it can also be further complicated due to their closer adherence. The SiNWs etched in *n*-Si are 2–6 times shorter compared with their counterparts on *p*-Si, which produces 3–5 times higher optical reflectance (Figure S1).

The SiNWs formed during the etching stage are grouped together in their upper parts. This is especially notable for the SiNWs, which are longer than 10 μm. Such a verticality violation is typical for the MACE-grown SiNWs. Their conglomeration occurs due to the significant length, as well as the presence of dangling bonds and electrostatic charges on the newly-formed surfaces. Deformations of this nature are especially pronounced for arrays of the nanowires with high aspect ratios [17].

The comparison of results obtained for wafers with different doping types suggests that *n*-type SiNWs have slightly larger diameters and significantly reduced lengths. This is more evident at high deposition times, at which the SiNWs based on *p*-Si have an almost tenfold increase in length comparing to their *n*-type counterparts. However, the dendrites growth occurs at the same rate, significantly complicating the etching process at its later stages. The difference in etching rates can be attributed to a lower concentration of free holes available for the Si oxidation, which is comprehensively discussed in the Supplementary Materials (Section 4).

SERS-activity of silver structures on/between SiNWs

Figure 2 shows a comparison of the SERS-spectra of 10^{-6} M R6G deposited on *p*- and *n*-type SiNWs samples with residual Ag. These spectra display the difference in SERS-activity for small silver particles (Figure 2, a, b) and silver dendrites (Figure 2, c, d) remained on/between SiNWs after the second MACE step. All the spectra present typical R6G Raman signatures, but the intensities of those collected from the dendrites structures are more extensive. It is generally accepted that the SERS enhancement mechanism is mostly electromagnetic in nature and highly determined by the structures nanoroughness and presence of nanoscale interparticle junctions [27]. The electromagnetic field near these structures localizes in narrow gaps and crevices between neighboring metal nanostructures. These areas are usually referred to the SERS hot-spots [28]. Electromagnetic enhancement is achieved due to the optical resonance between excitation light and oscillations of electron cloud in the metal. This process, named the localized surface plasmon resonance (SPR) leads to the Raman signal enhancement of the molecules proportionally to the fourth power of the absolute value of the local electric field amplitude.
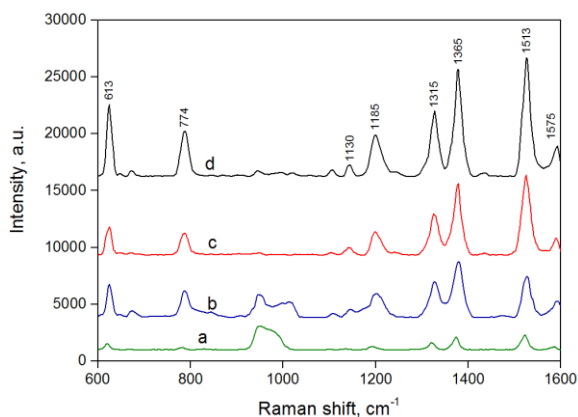
Figure 2 – SERS-spectra for 10^{-6} M R6G molecules adsorbed on Ag structures remained between SiNWs fabricated using (a, c) *n*-Si and (b, d) *p*-Si. SiNWs were etched for 60 min after the first MACE stage lasted for (a, b) 0.5 min and (c, d) 10 min.

As an outcome, organic molecules present in the SERS hot-spots dominate the resulting SERS spectrum, allowing for their effective detection even at extremely small concentrations. This is the reason why the silver dendrites that lay on the SiNWs and are characterized by multiple crossing trunks and sharp branches provide much better SERS-activity than the nanosized silver particles located between the nanowires. It should be noted that not only crossing and sharp branches generate a great field enhancement, but the particles composing these elements of dendrites are often located at marginally small distances from each other, providing large numbers of additional hot-spots. The lower SERS-intensity from the R6G molecules on the Ag particles between the SiNWs/*n*-Si (Figure 2, a) comparing to those between SiNWs/*p*-Si is explained not by their weaker SPR. In both cases, positioning the Ag particles between the SiNWs prevents direct adsorption of the analyte molecules in the hot spots. At the same time, the layer of longer SiNWs/*p*-Si, i.e. the Si nanostructures with highly developed surface area, is a substrate for anchoring more R6G molecules, which contribute in the moderate Raman signal enhancement. The prevalence of the Si nanostructures over the Ag ones in those samples is proved by not only the SEM images but also by the SERS-spectra, which contain a broad band around 980 cm^{-1} attributed to silicon oxide. Therefore, as the SiNWs surface area greatly affects the final metal particle distribution, longer nanowires are assumed to contribute to an increased Raman signal. Of course, if the Ag structures are laying on the SiNWs the dominating role in the SERS-effect is played by the hot spots.

Considering difference in the dendrites morphology for the SiNWs on *n*- and *p*-Si, we simulated the electric field distribution for the geometries extracted from the corresponding SEM images. Figure 3 reports these simulation results. It is seen from figure that the maximum electric field strength is nearly the same for both models, and the SERS-activity is expected to be equal. However, it is also well-seen that the more developed structure of the silver dendrites on the SiNWs/*p*-Si (Fig. 3b) enriched with nanosized branches ordered in chevron-like arrays is a source of much larger hot spots compared with SiNWs/*n*-Si (Fig. 3c).
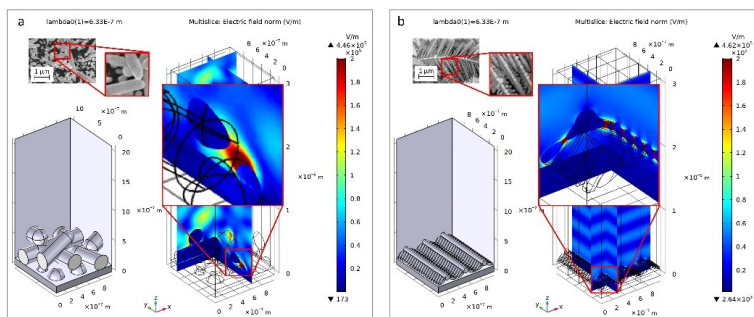
Figure 3 – Simulation results for silver dendrites remained on SiNWs fabricated on (a) *n*-Si and (b) *p*-Si. Insets show SEM top views of the silver dendrites used to model their structure.

Shelf life and detection limit of the SERS-active substrates based on SiNWs

Shelf life is an important characteristic of the SERS-active substrates. Silver-based substrates typically lose their effectiveness during long storage time because of oxidation of metallic nanostructures. In this work, we study the shelf life of the most efficient SERS-active sample composed of silver dendrites on the SiNWs/*p*-Si after the MACE silver deposition for 10 min and Si etching for 60 min. Two substrates were stored for one day and for a week in the air atmosphere of the closed fume hood and then R6G molecules were adsorbed on their surface from the 10^{-6} M solution (see Experimental section) for the SERS-measurements. Figure 4, a presents the resulting SERS-spectra.
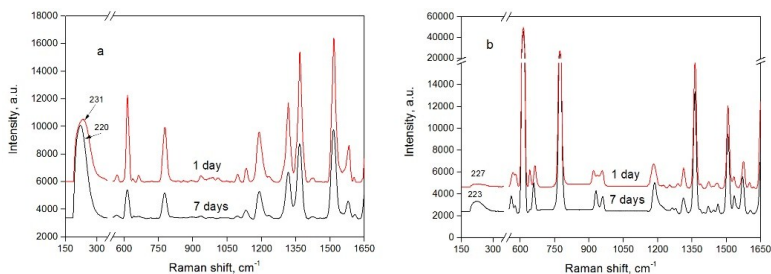

Figure 4 – SERS spectra for 10^{-6} M R6G adsorbed on (a) silver dendrites and (b) gold-silver dendrites. Silver dendrites remained in SiNWs etched in *p*-Si after the first MACE stage lasted for 10 min.

This is well-seen from figure that the R6G SERS-signal decreased twice after keeping the sample for seven days comparing with that stored for one day. An inhibition of the SERS-activity is caused by formation of silver sulfide, which characteristic band at 220–231 cm^{-1} is observed to be more intensive for the sample aged for a week.

7

Originally, the Ag$_2$S formation is associated with a poor chemical stability of the silver atoms. This negative effect can be overcome through protection of the silver structures with gold layer, which exhibits high chemical stability. In the present work, we exploit a higher gold redox potential than that of silver to deposit protective layer on the SERS-active substrate by the immersion technique. Figure 5 shows the SEM images and corresponding EDS elemental analysis of the silver dendrites remained on the SiNWs/p-Si after the gold plating. It is seen from Fig. 5b, d that the gold covers the external sprouts of the silver structures as tiny dendritic "flowers" and nanoparticles, which significantly improves chemical stability of the SERS-active substrates. This is proved by the presented SERS-spectra of R6G adsorbed on the Au/Ag dendrites/SiNWs/p-Si (Fig. 4b), which have nearly the same intensity and rather weak Ag$_2$S band both for one-day and week aged samples. The SERS-active substrates modified by Au deposition demonstrates successful and highly reproducible detection limit of R6G and DTNB molecules down to 10^{-9} M (Figure 6).
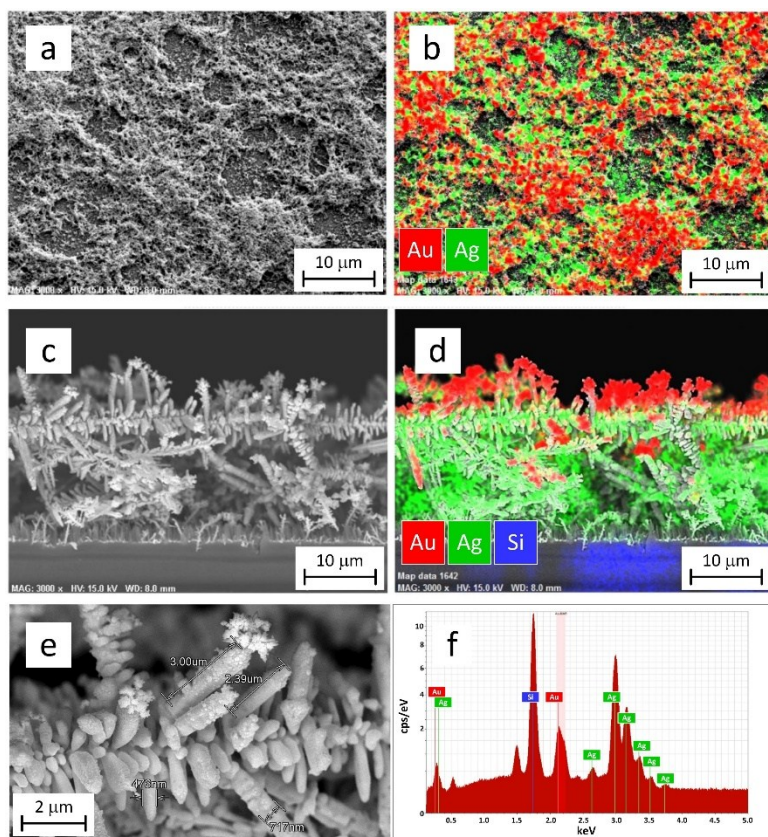

Figure 5 – SEM (a) top view and (c, e) cross-sections for gold and silver dendrites on SiNWs etched in p-Si after the first MACE stage lasted for 10 min. EDS (b, d) elemental distribution combined with the SEM images and (f) EDS spectrum for the gold and silver dendrites.
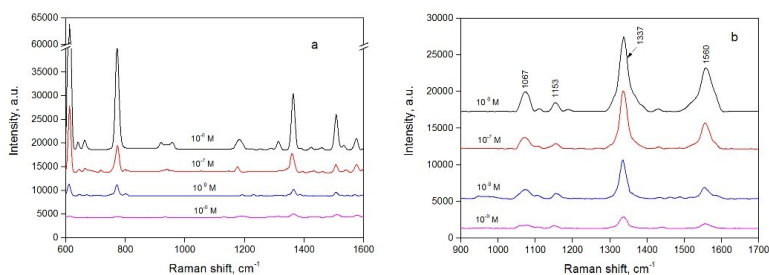
8

Figure 6 – SERS spectra for 10^{-6}–10^{-9} M (a) R6G and (b) DTNB adsorbed on gold-silver dendrites. Silver dendrites remained in SiNWs etched in *p*-Si after the first MACE stage lasted for 10 min.

CONCLUSIONS

This study have provided the comprehensive characterization of SiNWs fabricated by MACE of monocrystalline Si under different conditions. A two-step MACE have been carried out through (i) deposition of non-continuous Ag films on *n*- and *p*-Si wafers and (ii) subsequent chemical etching of Si initiated by Ag. The higher Ag deposition times on the first MACE stage have induced Ag films transition from densely packed quasi-spherical and elongated Ag nanoparticles to slightly branched dendrites. The SiNWs etched in *n*-Si have found to be 2–6 times shorter compared with their counterparts on *p*-Si, which resulted in 3–5 times higher optical reflectance. This is attributed to a lower concentration of free holes available in *n*-Si hampering its oxidation and dissolution during the second MACE stage. The thickening of the Ag film accompanied by the dendrites formation accelerates the SiNWs growth, which is caused by a higher rate of the Si oxidation due to redeposition of Ag within pores between the nanowires (see Section 5 in Supplementary Materials for more details). The silver structures remained on/between SiNWs based on both *n*- and *p*-Si have been found to promote SERS from organic molecules adsorbed on their surface. The Ag structures remained in the SiNWs/*p*-Si after the second MACE stage have facilitated two times higher SERS-signal from 10^{-6} M R6G compared with the SiNWs/*n*-Si. The activity of the SERS-substrates based on *p*-Si have been improved by their patterning with small gold dendrites due to the increased number of hot spots. The growth mechanism of these dendrites involves limited supply of electrons from SiNWs to the Au salt solution for the reduction of gold ions. The gold dendrites have also prevented the Ag_2S formation during the one-week samples storage in air. As the result, the SERS enhancement of these samples have remained stable, leading to the nanomolar detection limit of R6G and DTNB.

ACKNOWLEDGMENTS

References:

1. F. Wang, X. Gao, L. Ma, C. Yuan. Journal of Micro- and Nano-Manufacturing, **7**, 011001 (2019).
2. W. McSweeney, H. Geaney, C. O'Dwyer. Nano Research, **8**, 1395 (2015).
3. O. Salihoglu. Materials Research, **22**, 2 (2019)
4. M. R. Zamfir, H. T. Nguyen, E. Moyen, Y. H. Lee, D. Pribat. Journal of Materials Chemistry A, **1**, 9566 (2013)
5. F. Toor, W. Duan, B. Gao, M. Black. *Nanomaterials for Solar Cell Applications* (London, Elsevier, 2019) p. 699.
6. A. Sharstniou, S. Niauzorau, E. Chubenko, B. Azeredo, V. Bondarenko. MRS Advances, **2**, 3667 (2017).
7. X. Li, K. Tao, D. Zhang, Z. Gao, R. Jia, B. Wang, S. Jiang, Z. Ji, X. Liu. Electrochemistry Communications, **113** (2020).
8. Y. Lin, Y. Chen, C. Hsueh. Results in Physics, **12**, 244 (2019).
9. R. Lauridsen, T. Rindzevicius, S. Molin, H. Johansen, R. Berg, T. Alstrom, K. Almdal, F. Larsen, M. Schmidt, A. Boisen. Sensing and Bio-Sensing Research, **5**, 84 (2015).
10. S. Niauzorau, K. Girel, A. Sherstnyov, E. Chubenko, H. Bandarenka, V. Bondarenko. Phys. Status Solidi, **13**, 146 (2016).
11. K. Rajkumar, R. Pandian, A. Sankarakumar, R. Kumar. ACS Omega, **2**, 4540 (2017).
12. Z. Huang, N. Geyer, P. Werner, J. de Boor, U. Gösele. Adv. Mater., **23**, 285 (2010).
13. R. Milazzo, G. D'Arrigo, C. Spinella, M. Grimaldi, E. Rimini. Journal of the Electrochemical Society, **159**, 521 (2012).
14. O. Volovlikova, S. Gavrilov, A. Dronov, Y. Grishina, A. Belov. Sol. St. Phen., **213**, 103 (2014).
15. Y. Liu, G. Ji, J. Wang, X. Liang, Z. Zuo, Y. Shi. Nanoscale Res. Lett, **7**, 4540 (2012).
16. L. Cong, N. Lam, N. Giang, P. Kien, N. Dung, N. Ha. Mat. Sci. Semicon. Proc., **90**, 198 (2019).
17. M. Zhang, K. Peng, X. Fan, J. Jie, R. Zhang, S. Lee, N. Wong. J. Phys. Chem. C, **112**, 4444 (2008).
18. L. Li, C. Zhang, C. Tuan, Y. Chen, C. Wong. J. Micromech. Microeng., **28**, 055006 (2018).
19. Y. Hu, K. Peng, L. Liu, Z. Qiao, X. Huang, X. Wu, X. Meng, S. Lee. Scientific Reports, **4**, 3667 (2015).
20. A. Omer, Y. Yang, G. Sheng, S. Li, J. Yu, W. Ma, J. Qiu, W. Kolaly. Silicon, **12**, 231 (2019).
21. M. S. Schmidt, J. Hübner, A. Boisen. Adv. Mater, **24** (10), OP11-OP18 (2012).
22. S. Zavatski, N. Khinevich, K. Girel, S. Redko, N. Kovalchuk, I. Komissarov, V. Lukashevich, I. Semak, K. Mamatkulov, M. Vorobyeva, G. Arzumanyan, H. Bandarenka. Biosensors, **9**, 34 (2019).
23. D.T. Pierce, W.E. Spicer. Physical Review B, **5**, 3017 (1972).
24. A.D. Rakić, A.B. Djurišić, J.M. Elazar, M.L. Majewski. Applied Optics, **37**, 5271 (1998).
25. Q. Wee, J. Ho, S. Chua. ECS J. Solid State Sc., **3**, 192 (2014).
26. U. Vinzons, L. Shu, S. Yip, C. Wong, L. Chan, J. Ho. Nanoscale Res. Lett, **12**, 385 (2017).
27. D. Radziuk, H. Moehwald. Chem. Soc. Rev, **46**, 4042 (2017).
28. X. Han, W. Ji, B. Zhao, Y, Ozaki. Nanoscale, **9**, 4847 (2017).